AIAA AVIATION Forum
12-16 June 2023, San Diego, CA and Online
AIAA AVIATION 2023 Forum

10.2514/6.2023-4236

Control Surfaces for Supersonic Airfoil Using Co-flow Jet Active Flow Control

Zhijin Lei * Gecheng Zha †
Dept. of Mechanical and Aerospace Engineering
University of Miami, Coral Gables, Florida 33124
E-mail: gzha@miami.edu

Abstract

The effects using Co-Flow Jet (CFJ) active flow control method for 2-D and 3-D supersonic control surfaces with plain flaps, or rudders, are investigated. The goal is to increase the control efficiency of rudder on the vertical tails of supersonic civil transports (SST) at low speed and enable the possibilities to save energy expenditure. An approximate Concorde vertical tail profile is used as a baseline control surface for parametric trade study using a Reynolds-averaged Navier-Stokes (RANS) solver with Spalart-Allmaras (SA) model. A 3-rd WENO scheme for the inviscid flux is used to resolve the Navier-Stokes equations.

The 2-D and initial 3-D numerical studies indicate that, the CFJ equipped control surfaces can dramatically increase the lift coefficient and aerodynamic efficiency simultaneously compared with the original control surface with the same size of flap and deflection angle. However, due to the nature of low maximum thickness of airfoil and highly-swept planform, the 3-D effect is much stronger than the similar applications of wings with normal thickness.

In the 2-D simulation, at jet momentum coefficient of 0.08, the maximum lift coefficient is increased by 54.6% at side slip angle of 0°; when the jet momentum coefficient is increased to 0.16, the maximum lift coefficient increment is 76.5% compared with baseline. The 2-D CFJ airfoils show impressive efficiency at negative side slip angle conditions, where the maximum C_L increment compared with baseline is 157.4% at side slip angle of -7° with C_μ of 0.08. In the 2-D simulations, the Rudder-CFJ airfoil has extra lift enhancing effect, which is achieved by forming a stable separation region near the leading edge of the stabilizer, which increases the pressure difference over there. However, this lift enhancing mechanism no longer exists when it comes to the 3-D situation. The maximum lift coefficient increment with C_μ=0.08 in 3-D simulation is 37.1%, while the smallest loss of corrected aerodynamic efficiency achieved is 7.0% with a gain of maximum lift increment of 32.3%. Similar as the results on conventional airfoils, supersonic aircraft vertical tails equipped with CFJ show impressive potential to improve the control authority at low speed.

Nomenclature

AoA	Angle of Attack
AFC	Active Flow Control
C	Chord length
CFJ	Co-Flow Jet
VT	Vertical Tail
C_D	Drag coefficient

* Graduate Student
† Professor, ASME Fellow, AIAA associate Fellow

C_L	Lift coefficient
$C_{L,max}$	Maximum lift coefficient
C_M	Moment coefficient
C_p	Constant pressure specific heat
C_μ	Jet momentum coefficient, $\dot{m}_j\, U_j/(q_\infty\, S)$
D	Total drag on the rudder
$FASIP$	Flow-Acoustics-Structure Interaction Package
H_t	Total enthalpy
L	Total lift on the rudder
LE	Leading Edge
$\dot{m}$	Mass flow
M	Mach number
P	CFJ pumping power, $\dot{m}C_pT_{t,2}\ (\Gamma^{(\gamma-1/\gamma)}-1)/\eta$
P_c	Power coefficient, $P/0.5\rho_\infty {V_\infty}^3 S$
PR	Total pressure ratio, Γ
P_t	Total pressure
RANS	Reynolds-Averaged Navier-Stokes
Re	Reynolds number
s	Height of the vertical tail (halfspan)
TE	Trailing Edge
T_t	Total temperature
V_∞	Freestream velocity
ZNMF	Zero-Net Mass Flux
$(C_L/C_D)_c$	Aerodynamic efficiency corrected for CFJ, $C_L/(C_D+P_c)$
C_L^2/C_D	Productivity efficiency coefficient
$(C_L^2/C_D)c$	Productivity efficiency coefficient corrected for CFJ, $C_L^2/(C_D+P_c)$
c	Subscript, stands for corrected
j	Subscript, stands for jet
β	Sideslip angle
γ	Air specific heats ratio
η	CFJ pumping system efficiency, propeller efficiency
∞	Freestream density
δ	Deflection angle

1 Introduction

Supersonic Civil Transports (SST) remain a strong interest in the aviation research community and industry. Control surfaces like rudders, elevons and horizontal tails on such aircraft have their characteristics different from those on traditional commercial passenger jets.

"Conventional" SST designs, or those with a aerodynamic configuration similar to Concorde, use a large vertical tail to maintain their supersonic yaw stability, and a large rudder is introduced mainly to meet the requirement of control ability under cruise condition, where the drawback of low control force coefficients due to the low thickness and symmetric shape of the vertical tail profiles are cancelled out by the large absolute control force generated by high cruise speed of the aircraft. However, when it comes to takeoff and landing, the lower the flight speed is, the

more difficult it usually will be to maintain the control ability on such rudders.

The nature of infrequent need of this application makes active flow control (ACT) preferable to pure passive control methods, which provides no more than proportional control and frequently causes a drag penalty when the control is not expected[1]. AFC methods has a long history of lift enhancing and drag reducing application[2, 3, 4, 5, 6, 7, 8], as well as enhancing the control performance of vertical tails. Sweeping jet is a unique method that has been widely used in vertical tail applications[9] and actual flight[10], and considered by NASA to be preferred than the method of synthetic jets[10, 11], which are made up of "ejection-suction" cycles of flow produced by orifices induced by moving diaphragms inside the control surface. Another notable AFC approach is the concept of Co-Flow Jet (CFJ) developed by Zha *et al*[12], which is a zero-net mass flux (ZNMF) flow control methodology that does not need to extract mass flow from inlet bleed of compressor secondary flow, and thus independent from the engine cycle. The theoretical and actual reliability of CFJ has been intensively validated both numerically and experimentally [12, 13, 14, 15, 16, 17, 18, 7, 19, 20, 21, 22], and great ability and potential to achieve radical lift augmentation, stall margin increase and drag reduction have been observed. Zhang *et al* [23] conducted a 2-D numerical simulation to study a new aircraft control surfaces using CFJ airfoils. Xu *et al* studied the energy expenditure based on Zhang *et al*'s results[24], and used 3-D Improved Delayed Detached Eddy Simulation (IDDES) turbulence model to simulate a 3-D vertical tail of a commercial passenger jet with airfoil of NACA0012[25].

There are not many published researches on applying AFC to wings or tails with thin profile. Mavris *et al*[26] employed circulation control(CC) flow control to enhance HSCT low speed lift coefficient based on the work of Englar[27]; with certain configurations, the CC method can reduce the takeoff field length by 31%, the liftoff speed by 11%, and the obstacle height speed by 10%. However, the jet flow of CC comes from engine bleed, which happen to be difficult to obtain during takeoff, when the engines need maximum mass flow for maximum thrust, and as well landing, when all the engines are expected idle. Lei *et al*[28, 29] numerically simulated applying CFJ on 2-D and 3-D flapped delta wings, and receive 50% lift enhancement and maintained lift-drag ratio at low speed. This method has been numerically proved to have a wide effective range of airfoil shapes[30]. The purpose of this paper is to apply CFJ to the vertical tail designed for a typical Concorde-like supersonic civil transport, and improve its low-speed control ability.

1.1 The Co-Flow Jet Airfoil for Control Surfaces

In a CFJ airfoil, an injection slot near the leading edge (LE) and a suction slot near the trailing edge (TE) on the airfoil suction surface are created. As shown in Fig.1, a small amount of mass flow is drawn into the suction duct, pressurized and energized by the micro compressor, and then injected near the LE tangentially to the main flow via an injection duct. The whole process does not add any mass flow to the system and hence is a zero-net-mass-flux(ZNMF) flow control.

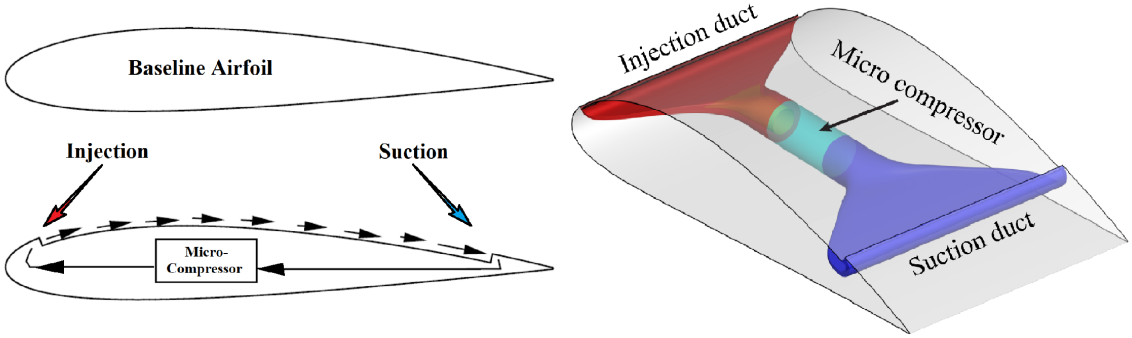

Figure 1: Schematic plot of a typical CFJ airfoil.

2 CFJ Parameters

This section lists important parameters to evaluate aerodynamic performance of a CFJ airfoil.

2.1 Jet Momentum Coefficient

The jet momentum coefficient C_μ is a parameter used to quantify the jet intensity. It is defined as:

$$C_\mu = \frac{\dot{m}U_j}{\frac{1}{2}\rho_\infty {U_\infty}^2 S} \tag{1}$$

where $\dot{m}$ is the injection mass flow, V_j is the mass-averaged injection velocity, ρ_∞ and V_∞ denote the free stream density and velocity, and S is the planform area.

2.2 Power Coefficient

CFJ is implemented by mounting a pumping system inside the wing that withdraws air from the suction slot and blows it into the injection slot. The power consumption is determined by the jet mass flow and total enthalpy change as the following:

$$P = \dot{m}(H_{t1} - H_{t2}) \tag{2}$$

where H_{t1} and H_{t2} are the mass-averaged total enthalpy in the injection cavity and suction cavity respectively, P is the Power required by the pump and $\dot{m}$ the jet mass flow rate. Introducing P_{t1} and P_{t2} the mass-averaged total pressure in the injection and suction cavity respectively, the pump efficiency η, and the total pressure ratio of the pump $\Gamma = \frac{P_{t1}}{P_{t2}}$, the power consumption is expressed as:

$$P = \frac{\dot{m}C_pT_{t2}}{\eta}(\Gamma^{\frac{\gamma-1}{\gamma}} - 1) \tag{3}$$

where γ is the specific heat ratio equal to 1.4 for air, the power coefficient is expressed as:

$$P_c = \frac{P}{\frac{1}{2}\rho_\infty V_\infty^3 S} \tag{4}$$

2.3 Corrected Aerodynamic Efficiency

The conventional wing aerodynamic efficiency is defined as $(\frac{C_L}{C_D})_c$. For the CFJ wing, the ratio above still represents the pure aerodynamic relationship between lift and drag. However, since CFJ active flow control consumes energy, the ratio above is modified to take into account the energy consumption of the pump. The formulation of the corrected aerodynamic efficiency for CFJ control surfaces is:

$$(\frac{L}{D})_c = \frac{C_L}{C_D + P_c.} \tag{5}$$

where P_c is the power coefficient, L and D are the lift and drag generated by the CFJ wing. The formulation above converts the power consumed by the CFJ into a force $\frac{P}{V_\infty}$, which is added to the aerodynamic drag D. If the pumping power is set to 0, this formulation returns to the aerodynamic efficiency of a conventional control surface.

3 Numerical Algorithm

The in-house high-accuracy CFD code Flow-Acoustics-Structure Interaction Package(FASIP), which has been intensively validated for CFJ airfoil and internal flow simulations[4, 7, 13, 14, 16, 17, 18, 31, 32, 33, 34], is used to conduct this numerical simulation. The 3-D Reynolds averaged Navier-Stokes (RANS) equations with one-equation Spalart-Allmaras(SA) turbulence model is used. A 3rd order WENO scheme for the inviscid flux and a 2nd order central differencing for the viscous terms are employed to discretize the Navier-Stokes equations. The low diffusion E-CUSP scheme used as the approximate Riemann solver suggested by Zha *et al* [35] is utilized with the WENO scheme to evaluate the inviscid fluxes. Implicit time marching method using Gauss-Seidel line relaxation is used to achieve a fast convergence rate[36].

To achieve zero-net mass-flux with the CFJ flow control automatically in the solver, the injection mass flow is iterated to be made equal to the mass flow entering the suction slot. Additionally, the jet strength must be controlled in order to reach the prescribed C_μ. This is achieved by iterating the jet total pressure until the C_μ value is within 5% of the prescribed value. At the suction, the suction mass flow is matched to the injection mass flow by iterating the static pressure at the suction cavity. The process is iterated throughout the simulation until the specified momentum coefficient is achieved and the injection and suction mass flow match.

4 Definition of Geometries, Meshes and Flow Conditions

4.1 2-D Baseline and CFJ Vertical Tail Profiles

The baseline 2-D vertical tail is built as a simplified vertical tail of Concorde. As a reasonable approximation, the baseline vertical tail uses a single symmetric airfoil of thickness 4.0%, the reference shape of which captured from the antenna blueprint of Technical Specification Manual of Concorde [37], as shown in Fig. 2:

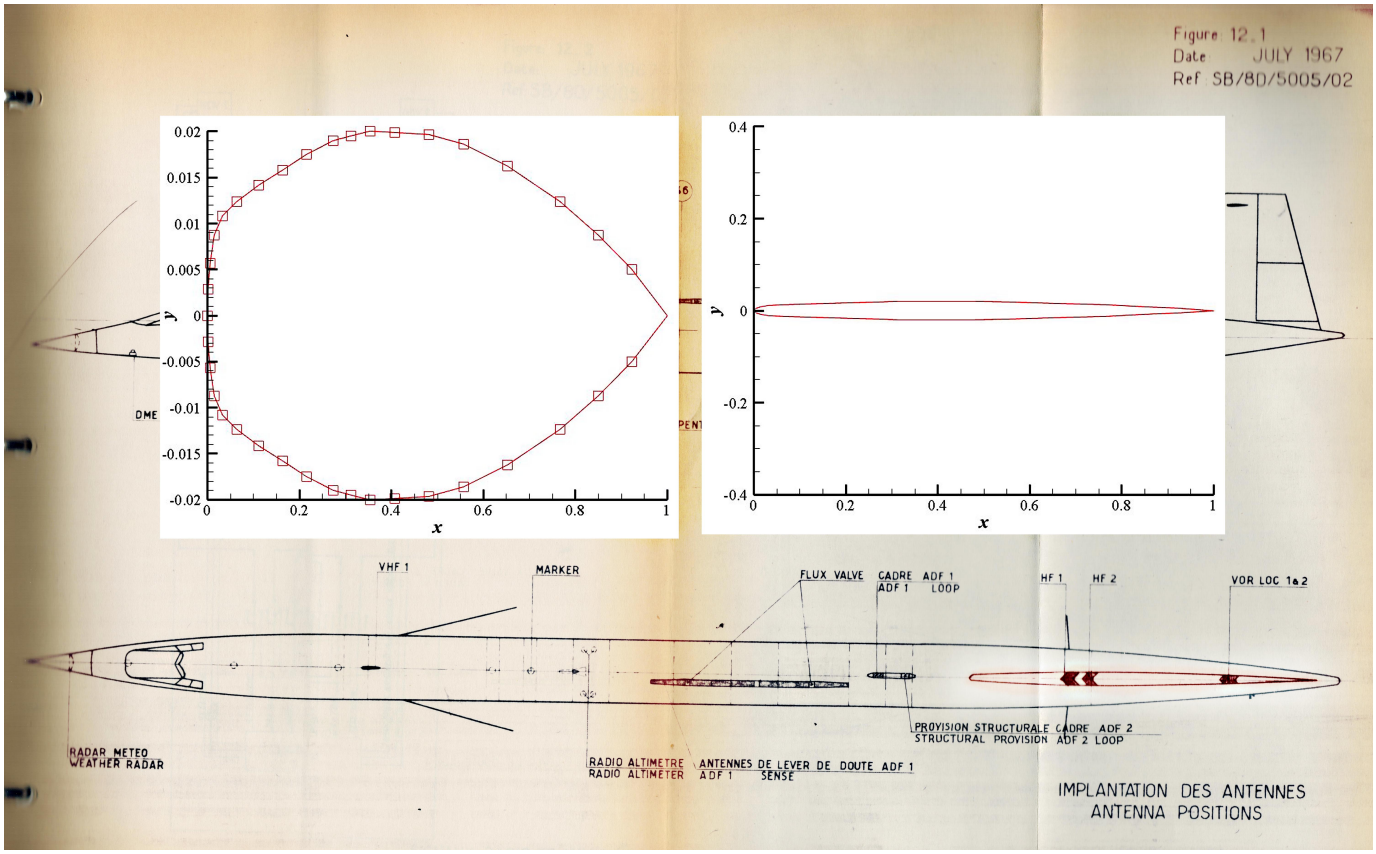

Figure 2: Baseline VT wing profile geometry from[37].

According to the dimensions shown in Fig. 3(a) [37], a simplified baseline vertical tail planform is defined as the highlighted trapezoid, which has a LE swept angle of 42°, a height (span) of 5788.2 mm, a mean aerodynamic chord (MAC) of 7448.2 mm, a 20% chord of flap (rudder) length and a flap deflection angle of 30°, as shown in Fig. 3(d). The deflected mode of the control surface is geometrically simplified by deflecting the root and tip profile at 20% chord-length axis point separately and bridging the two profiles together.

Fig. 3(b) and (c) shows the planform shape differences between original (b) and simplified VT(c).

According to the highlighted dimensions from [31] shown in Fig. 3(a), a simplified 3-D baseline vertical tail model including stabilizer and rudder is made, which is tapered and has a LE swept angle of 42°. Fig. 3(b) and (c) shows the planform shape difference between original (b) and simplified VT(c). In this rudder effect enhancement study, an initial rudder deflection angle of 30° is given, as shown in Fig. 3(d), where stabilizers are shown in gray and rudders are shown in blue.

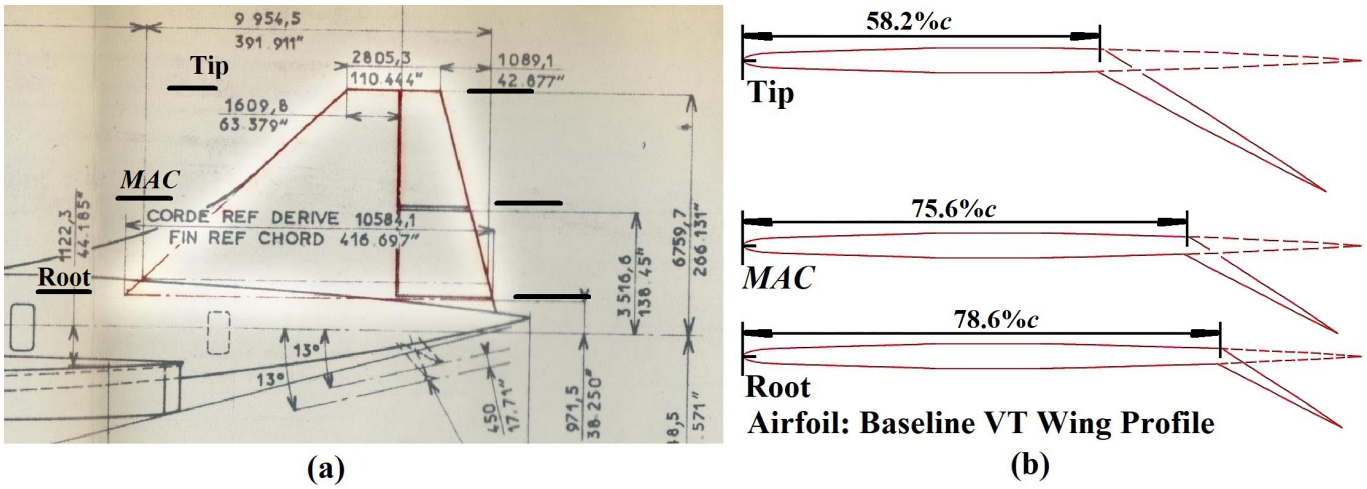

Figure 3: Dimension of a simplified Concorde vertical tail(a) and comparison of non-dimensionized flapped 2-D profiles at varied non-dimensionized heights(b), rudder deflection angle of 30°(d).

The 2-D profile of the tip and root of this simplified wing is studied, as shown in Fig. 3(a). For the airfoil of root, the local flap (rudder) length is 21% of local chord length; while for the airfoil of tip, the local flap (rudder) length is 42% of local chord length. The simulations are conducted under the flow conditions of freestream $Re_\infty = 3.43 \times 10^7$ (based on root chord length) and 8.22×10^6 (based on tip chord length), M varies from 0.1 to 0.2, and sideslip angle β varies from -7° to 7°. The zero gradient condition is applied to farfield in the span direction away from the tip. The total pressure, total temperature and flow angle are specified at the farfield inlet and the static pressure is specified at the outlet to match the freestream Mach number. The outer root domain uses the symmetry boundary condition. For all solid wall surfaces, the no-slip wall boundary condition is used. The wall treatment suggested in [38] to achieve the 3rd order accuracy is employed. Constant static pressure is also used downstream inside the CFJ suction cavity.

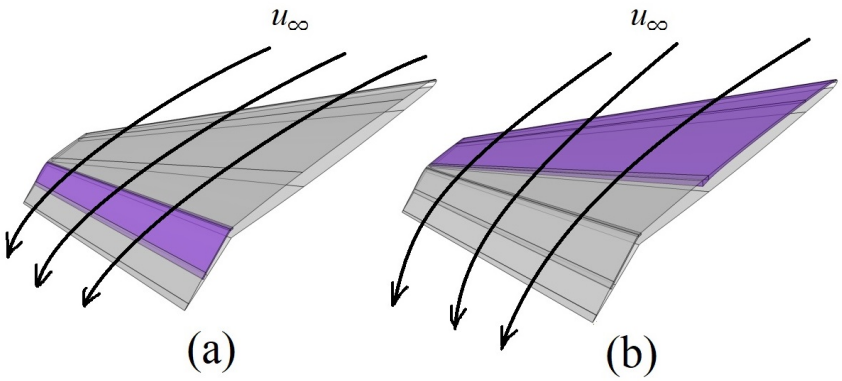

Figure 4: Schematic of two CFJ configurations.

Two CFJ locations are depicted as in Fig. 4, namely Rudder-CFJ-VT(Fig. 4(a)) and Rudder-Stabilizer-CFJ-VT(Fig. 4(b)), where CFJ-covered regions are shown in purple.

The 2-D meshes at roots and tips are shown in Fig. 5 and Fig. 6 respectively. The computational domain is meshed using O-type grid with the mesh size of 24,000 cells (2.4k × 100). Mesh in the streamwise direction is

refined to precisely picture the shape of thin airfoil and related CFJ-duct openings. Radial farfield has 20 times of reference length(mean aerodynamic chord length) MAC length. A mesh dependent analysis is conducted by doubling the number of grid points in $i-$ and $j-$ direction respectively. The result indicates that, the 2-D baseline mesh is reasonably converged and thus considered acceptable.

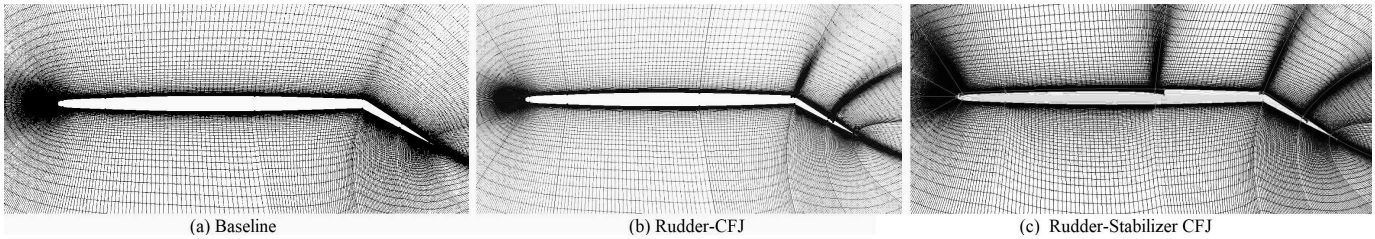

Figure 5: 2-D Meshes of VT profile with rudder deflection angle of 30° at root symmetric plane.

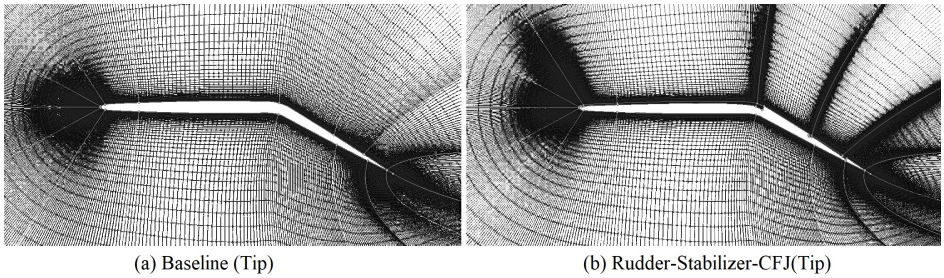

Figure 6: 2-D Meshes of VT profile with rudder deflection angle of 30° at tip symmetric plane.

4.2 Baseline 3-D Control Surface

The baseline 3D vertical tail is built as a simplified vertical tail of Concorde. The profile is defined in Fig. 2 as shown above. According to the dimensions shown in Fig. 7(a) [37], a simplified baseline vertical tail planform is defined as the highlighted trapezoid, which has a LE swept angle of 42°, a height (span) of 5788.2 mm, a mean aerodynamic chord (MAC) of 7448.2 mm, a 20% chord of flap (rudder) length and a flap deflection angle of 30°, as shown in Fig. 7(d). The deflected mode of the control surface is geometrically simplified by deflecting the root and tip profile at 20% chord-length axis point separately and bridging the two profiles together.

Fig. 7(b) and (c) shows the planform shape differences between original (b) and simplified VT(c).

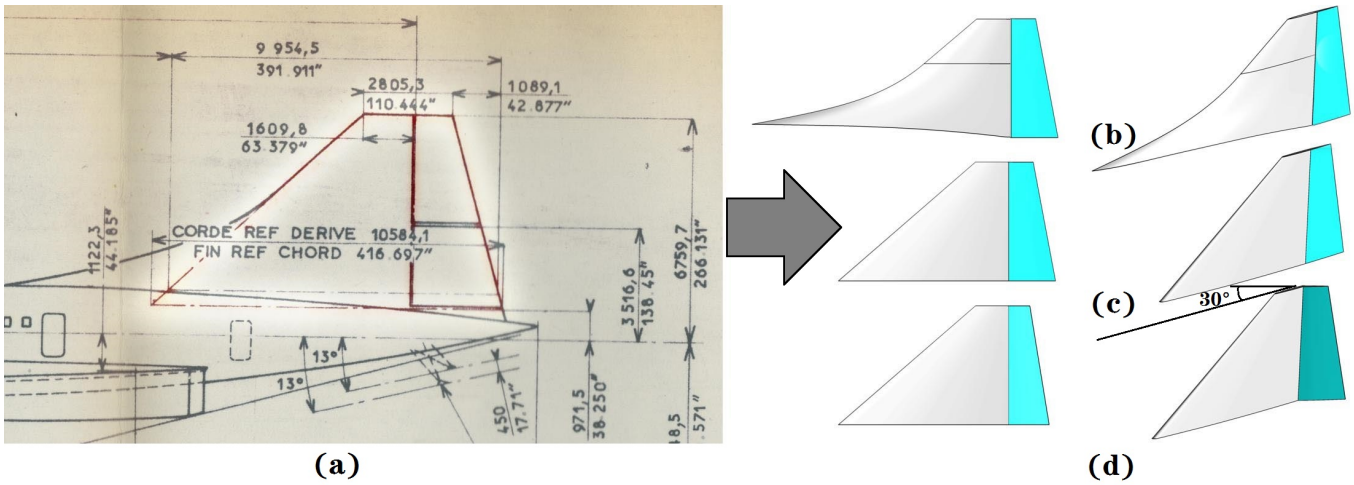

Figure 7: Dimension of a simplified Concorde vertical tail(a); a comparison between real Concorde VT(b), simplified model(c) and simplified model with rudder deflection angle of 30°(d).

The 3-D mesh topology is shown in Fig. 8. The computational domain is meshed using O-type grid with the mesh size of 6.80 million cells (1.03k $\times$ 60 $\times$ 100). Mesh in the streamwise direction is refined to precisely picture the shape of turning points and spaces for related CFJ-duct openings. The radial farfield has a distance of 21 times of the reference length (MAC) to the geometry, while the spanwise farfield has a distance of 10 times of the rudder height to the rudder tip.

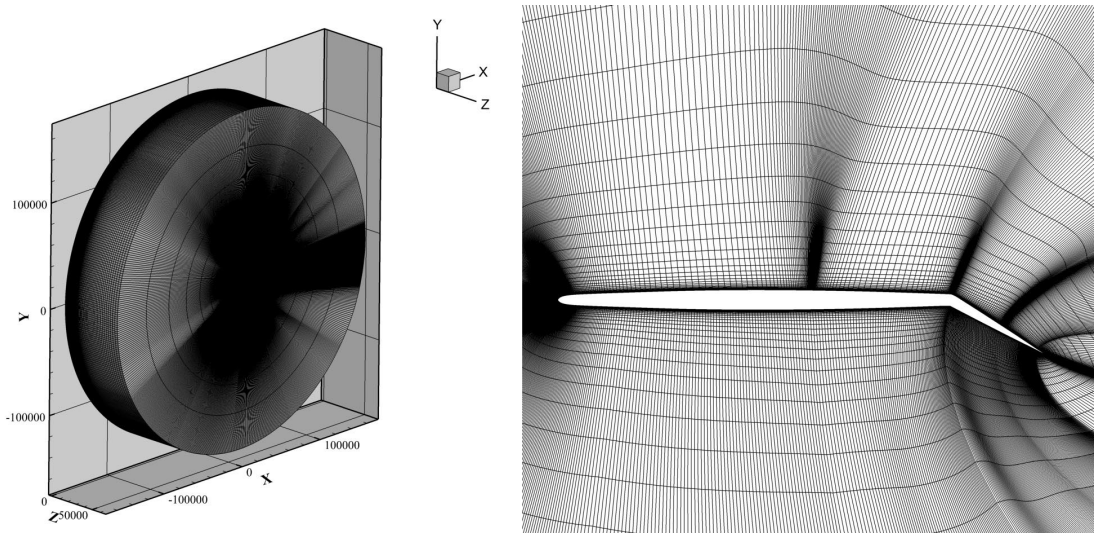

(a) Mesh in real dimension (mm)

(b) Mesh at root symmetric plane

Figure 8: 3-D Mesh calculation zone(a) and surface mesh of root symmetric plane(b).

The zero gradient condition is applied to farfield in the span direction away from the tip. The total pressure, total temperature and flow angle are specified at the farfield inlet and the static pressure is specified at the outlet to match the freestream Mach number. The symmetry boundary condition is applied to both the outer root domain and the farfield parallel to the tip surface. The no-slip wall boundary condition is applied to all solid wall surfaces, as shown in Fig. 9. The wall treatment suggested in [38] is employed to achieve the 3rd order accuracy.

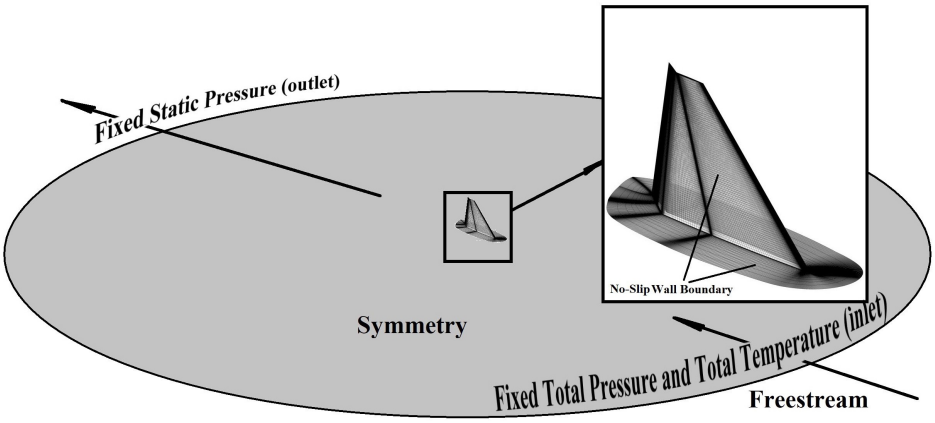

Figure 9: Definition of outer boundary conditions in the domains.

A mesh dependence analysis is conducted by doubling the number of grid points in $i-$, $j-$, and $k-$ direction respectively under the computational conditions of freestream $Re_\infty = 3.43 \times 10^7$ (based on MAC), $U_\infty = 68$m/s (Mach Number of 0.2), and sideslip angle β=0°. The mesh dependence results show that the maximum discrepancy for the lift coefficient is 0.43% and for the drag is 0.8%, which indicates that the baseline mesh is reasonably converged and is thus acceptable.

4.3 Definition of CFJ Control Surfaces

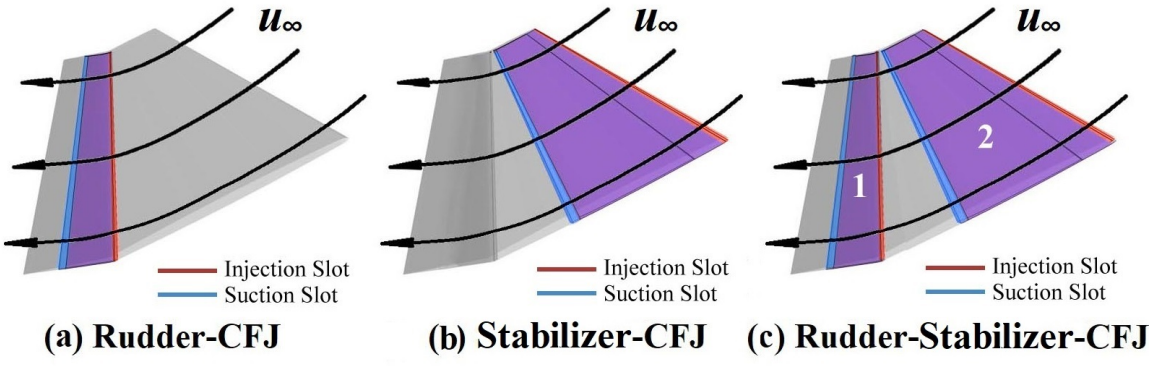

Figure 10: Three CFJ distribution locations with rudder deflection angle of 30°.

Three types of CFJ distribution locations are depicted as in Fig.10, namely "Rudder-CFJ"(Fig. 10(a)) "Stabilizer-CFJ"(Fig. 10(b)) and "Rudder-Stabilizer-CFJ"(Fig. 10(c)), where suction surfaces covered by CFJ jet flow are shown in purple. For Stabilizer-CFJ, the injection slot exit is located at 1%C from LE and the suction slot inlet is located at 51%C from LE. For Rudder-CFJ, the injection slot starts from 80%C from LE(which is 2%C from rudder turning point) and the suction slot inlet is located at 90%C from LE(which is 12%C from rudder turning point). Based on the conclusion of the spanwise CFJ distribution study [39], the swept effect study of jet flow[40] and the previous 3-D delta wing study[28], an alternative Rudder-Stabilizer-CFJ-2 model is created to achieve similar lift enhancing effect with reduced CFJ-covered suction surface area, as shown in Fig. 11(b), where the

front CFJ set covers 54% of the height at LE(from 32%H to 86%H) and back CFJ set covers 10% of the height at both LE and TE.

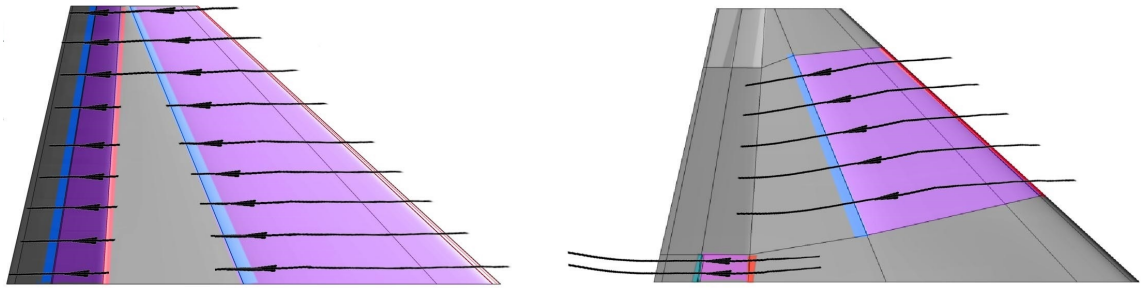

(a) Rudder-Stabilizer-CFJ (b) Rudder-Stabilizer-CFJ-2

Figure 11: CFJ distribution and expected streamline of Rudder-Stabilizer-CFJ(a) and a proposed alternative Rudder-Stabilizer-CFJ-2(b).

For Stabilizer-CFJ, the injection slot size is 12.0%C at all spanwise locations, and the suction slot size is 26.8%C at all spanwise locations, which is the maximum possible size allowed due to the geometrical limit. For Rudder-CFJ, the injection slot size is 6.0%C at all spanwise locations and the suction slot size is 10.0%C at all spanwise locations. In all CFJ geometries, the injection and suction slots in the opposite side will lead to a small gap, which is considered as insignificant to affect the aerodynamic performance and thus not simulated in this study. For boundary conditions inside the CFJ duct, constant static pressure is also used downstream inside the CFJ suction cavity, and the total pressure in the injection duct is iterated to meet the requirements of C_μ. The suction slot width and orientation are defined according to the best performing configuration of Liu *et al*[33]. The computational flow conditions of CFJ are identical to that of the baseline geometry, where the freestream Re_∞ equals to 3.43×10^7 (freestream velocity 68m/s, Re_∞ based on MAC), the freestream velocity U_∞ = 34m/s (Mach Number of 0.1) and 68m/s (Mach Number of 0.2), and the sideslip angle β=0°.

5 Control Surface Cut-Off Profile Study

The 2-D results include three major parts: 1) Study on the optimal CFJ location on a thin tapered vertical tail with a constant rudder deflection angle of 30°; 2) Study on the C_μ influence; and 3) Study on the influence of sideslip angle at a constant maximum possible C_μ of 0.08.

The C_L, C_D, P_c, C_L/C_D and $C_L/C_(D,c)$ of four root profiles when the rudder is deflected for 30°, freestream Mach number = 0.2 and CFJ C_μ = 0.08 are listed in Table. 1 as a general overview of the 2-D performances. The result indicates that, Rudder-CFJ can increase C_L by 54.6% at around 30% cost of corrected aerodynamic efficiency $(L/D,c)$ loss, while the combined Rudder-Stabilizer-CFJ can increase C_L by only 24.2% but at the cost of lower energy expenditure.

The 2-D flowfields of Baseline, Rudder-CFJ and Rudder-Stabilizer-CFJ and isentropic Mach number distributions along the geometry surface of Baseline, Rudder-CFJ and Stabilizer-CFJ with rudder deflection angle δ=30° at Ma=0.2, CFJ C_μ = 0.08, sideslip angle β=0° are compared in Fig. 12. It can be clearly seen that, the extra lift enhancement of Rudder-CFJ comes from the stable separation layer over the front part of the stabilizer suction surface. The CFJ on the rudder(b) introduced and restrains the separation, which introduces extra pressure difference, while a solo CFJ on the stabilizer can only create a slight pressure drop over suction surface via jet effect.

Table 1: Comparison of C_L, $C_L/C_{D,c}$ and other performances, β=0°, δ=30°, freestream Ma=0.2, CFJ C_μ=0.08.

Type	C_L	C_L Improve	C_D	P_c	C_L/C_D	$C_L/C_{D,c}$	$C_L/C_{D,c}$ Change
Baseline	0.981	-	0.056	0	17.377	17.377	-
Rudder-CFJ	1.517	54.6%	0.073	0.054	20.64	11.88	-31.6%
Stabilizer-CFJ	1.218	24.2%	0.039	0.047	31.30	14.19	-19.4%
Rudder-Stabilizer-CFJ	1.483	51.2%	0.050	0.030	29.37	18.41	5.97%

When CFJ is applied to both locations, this Rudder-CFJ-introduced lift enhancement still exists but is weakened by the other CFJ, as shown in (c). The isentropic Mach number distribution shown in (d) further illustrates this mechanism.

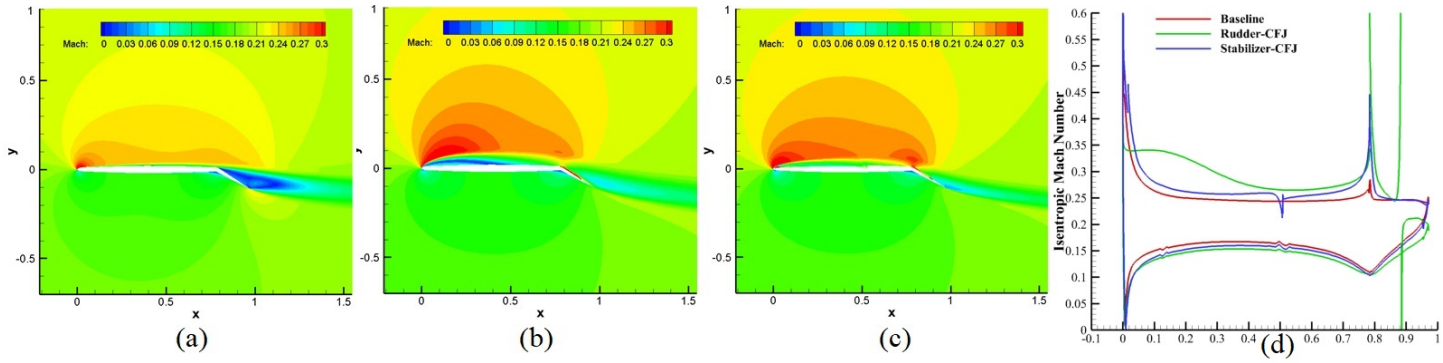

Figure 12: The flowfield around Baseline control surface(a), Rudder-CFJ(b) and Both-CFJs(c), freestream Mach number = 0.2, C_μ = 0.08. The isentropic Mach number distribution of Baseline, Rudder-CFJ and Stabilizer-CFJ is shown in (d).

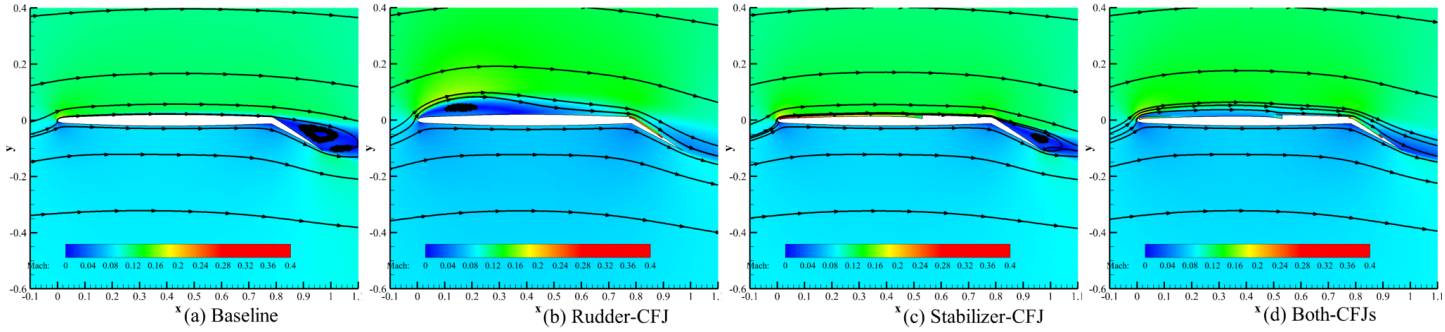

Figure 13: The streamline around baseline control surface(a), Rudder-CFJ(b), Stabilizer-CFJ(c) and Rudder-Stabilizer-CFJ(d), which will be also mentioned as Both-CFJs for simplicity, freestream Mach number = 0.1, C_μ = 0.08.

When the freestream Mach number is dropped to 1.0, this Rudder-CFJ-caused lift enhancing effect becomes even stronger. The Mach number contours of Baseline, Rudder-CFJ , Stabilizer-CFJ and Rudder-Stabilizer-CFJ with rudder deflection angle δ=30°, freestream Ma=0.1 and CFJ C_μ = 0.08 are compared in Fig. 13. It can be seen that, at such a thin airfoil, Stabilizer-CFJ cannot eliminate all separations over suction surface. The Rudder-

Stabilizer-CFJ eliminates both separation regions around the airfoil, which reduces both aerodynamic drag and energy expenditure introduced by CFJ system, but it undermines the lift enhancement effect mentioned above and leads to a slightly reduced lift performance.

5.1 Influence of C_μ

To study the effect of the jet intensity and its limit due to the nature of narrow injection and suction duct, five C_μs, namely 0.02, 0.04, 0.06, 0.08 and 0.16 are simulated based on three CFJ configurations with δ=30°, freestream Mach number = 0.1. The aerodynamic performances of all 2-D control surfaces are plotted versus C_μ in Fig. 14, which shows a quite complicated picture of the lift coefficient(a) and corrected aerodynamic efficiency(b), indicating that too many geometrical and aerodynamic factors are influencing the situation. A general conclusion is that, Rudder-CFJ tends to increase lift as well as drag, while Stabilizer-CFJ tends to reduce both. A combination of both CFJs (where C_μ is separated equally) has the lowest jet speed at injection slot, and thus lowest energy loss by CFJ, or power coefficient, as shown in Fig. 14(c); with this advantage, the Both-CFJs configuration wins the highest $C_L/C_{D,c}$, as shown in Fig. 14(f); at the maximum studied C_μ of 0.16, the value is 19.371, which is an increase of 11.5% compared with the baseline, while the lift enhancement is still among the highest ones with most of the C_μs applied. At the same C_μ, Stabilizer-CFJ generates the largest C_L of 1.731 among all, which is a 76.5% increment compared with baseline, but at the cost of a 45% decrease of $C_L/C_{D,c}$; meanwhile, C_L provided by Rudder-Stabilizer-CFJ is 1.646, still a 67.8% increase. Fig. 15 shows the flowfields at two C_μs.

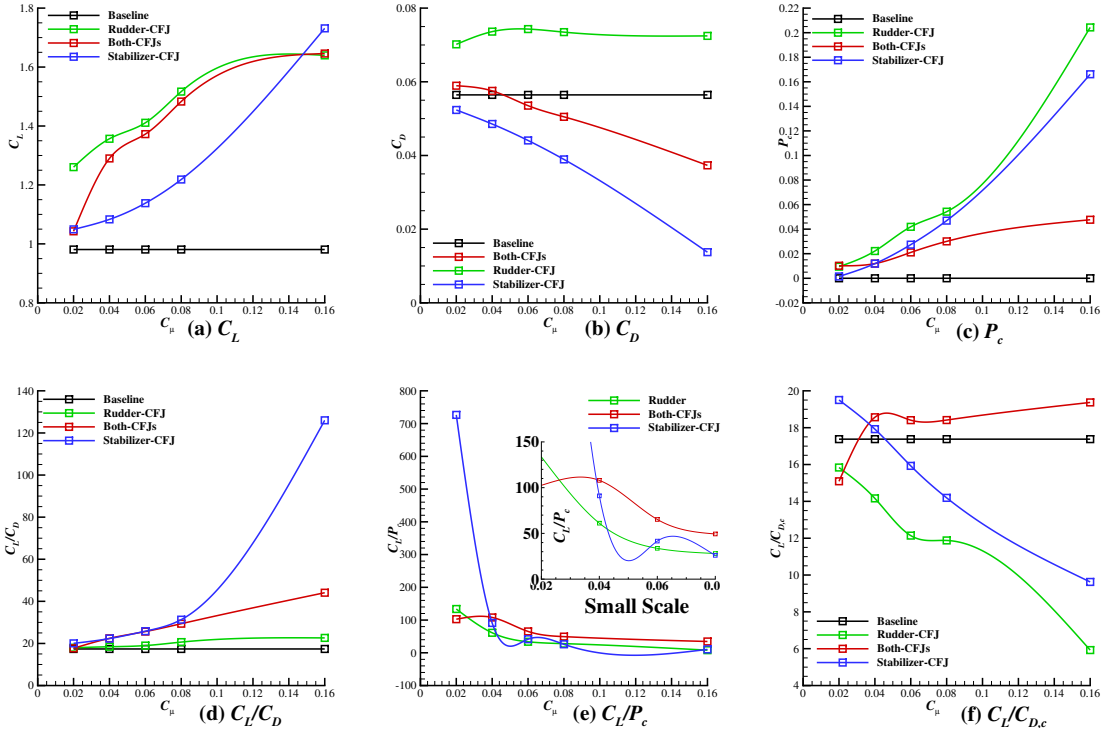

Figure 14: Aerodynamic coefficients of baseline and varied CFJ airfoils versus increased C_μ, Ma=0.1, Flap deflection angle δ=30°. The curves are interpolated by spline.

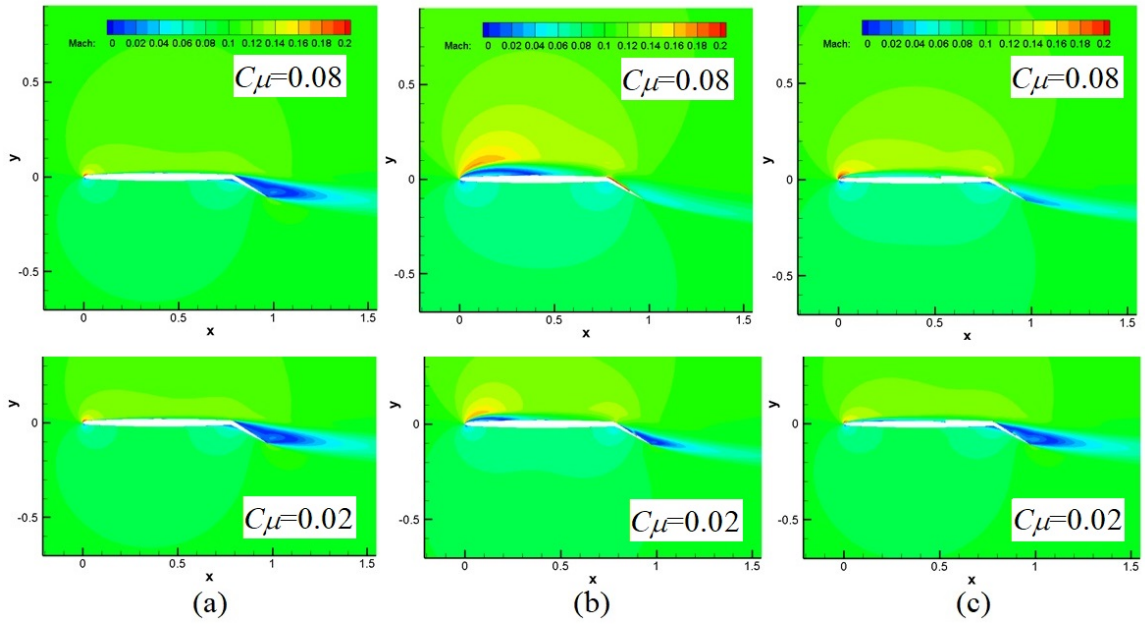

Figure 15: Mach number contours around Baseline(a), Rudder-CFJ(b) and Rudder-Stabilizer-CFJ(c) at C_μ=0.02 and 0.08, freestream Ma=0.1, and Flap deflection angle δ=30°.

For Rudder-Stabilizer-CFJ airfoils, the C_μ distribution among the two CFJ sets could influence the performance. Table. 2 shows an example of how this factor can differs the final result as the total C_μ remains unchanged. A general conclusion is that, around the working point of the interest of this paper, uniformly distribution results in both maximum C_L and maximum $C_L/C_{D,c}$.

Table 2: Comparison of C_L, $C_L/C_{D,c}$ and other performances of Rudder-Stabilizer-CFJ, β=0°, δ=30°, as the C_μ weight of two CFJ sets varies. C_μ in total is maintained at 0.08.

$C_{\mu,Stabilizer}$	$C_{\mu,Rudder}$	C_L	C_D	P_c	C_L/C_D	C_L/P_c	$C_L/C_{D,c}$
0.06	0.02	1.143	0.0448	0.041	25.508	27.616	13.260
0.05	0.03	1.352	0.0465	0.028	29.045	48.701	18.194
0.04	0.04	1.483	0.051	0.030	29.369	49.368	18.414

5.2 Influence of Sideslip Angle

The comparison of aerodynamic performances between baseline and three CFJ airfoils with a sideslip angle β range of -7° to 7° are shown in Fig. 16. The CFJ C_μ = 0.08, freestream Ma=0.1, and flap deflection angle δ=30°.

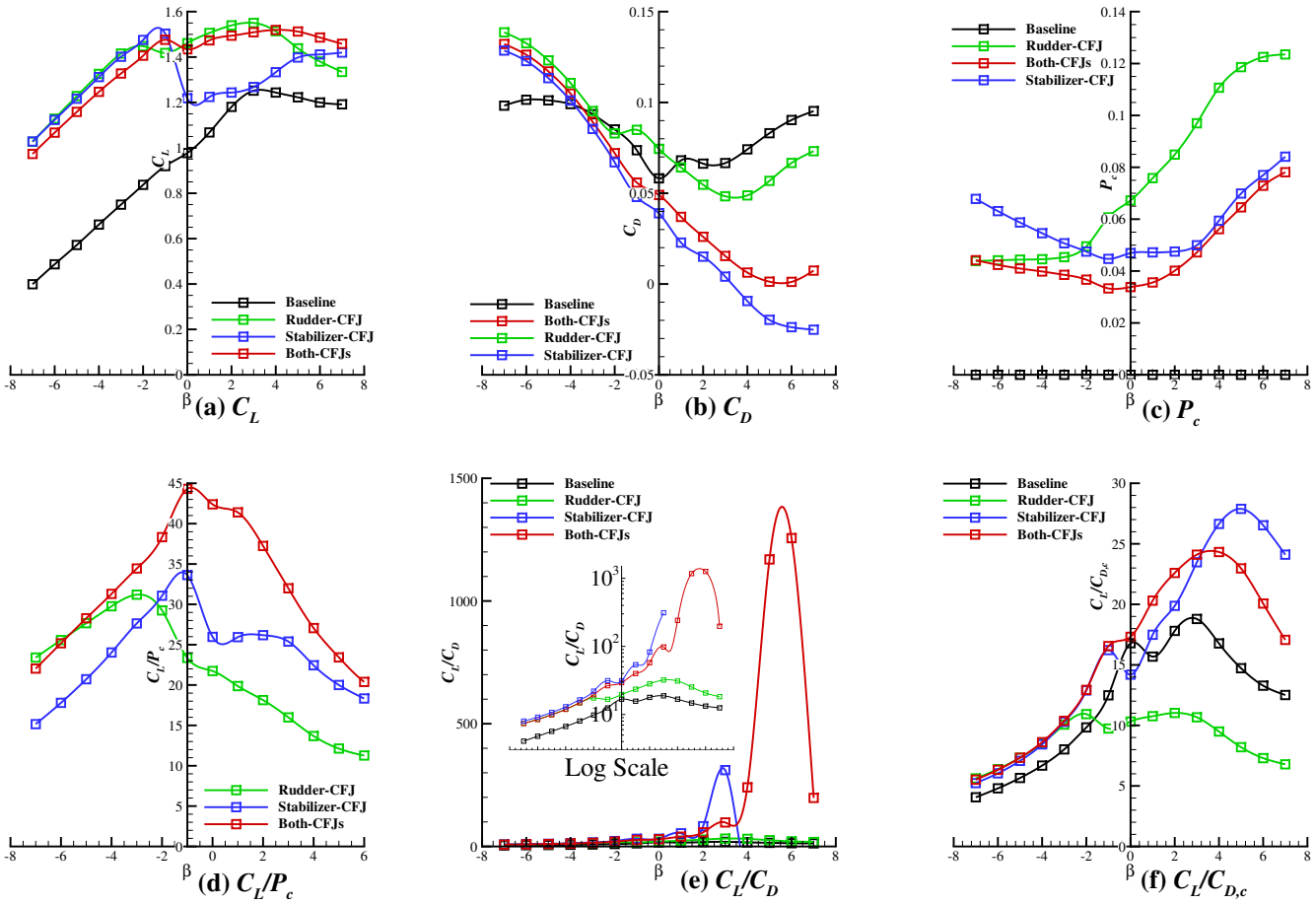

Figure 16: Comparison of flowfields between baseline and 2 CFJ-VT airfoils with a sideslip angle β of -7°, where C_μ=0.08, M=0.1, Flap deflection angle δ=30°.

Compared with the results of 2-D CFJ-thick-airfoil study conducted by Zhang *et al*[23], not only the lift and drag performance of baseline airfoil is quite different, but also the influence of CFJ is different as well. All CFJ airfoils provides a tremendous improvement of lift and $C_L/C_{D,c}$ at the negative β region, but all of them experiences a sudden drop of lift when β is increased to near zero, which is the supposed normal flight condition. With a positive β, the lift enhancement effect of CFJ still always exists, but significantly weakened, especially for the Stabilizer-CFJ. At β=-7°, Rudder-CFJ improves C_L from 0.399 of baseline to 1.027, which is a 157.4% increase; at the same time, the $C_L/C_{D,c}$ of Rudder-CFJ is 5.626, which is still 38.5% higher than that of baseline. When it comes to β=7°, due to the small drag coefficient achieved by the CFJ set on the stabilizer, the Stabilizer-CFJ has a $C_L/C_{D,c}$ of 24.10, which is 92.6% larger than that of baseline; however, due to the extremely large energy loss from pumping power, the Rudder-CFJ only produces a $C_L/C_{D,c}$ of 6.785, which is only 54.23% of the baseline. Despite that there is still a 19.8% increase of lift coefficient, maintaining this lift enhancement using Rudder-CFJ will be much more energy-consuming.

The 2-D performances of tip are also analysed, which provides similar results except that the separation region is further increased. However, the most effective lift enhancing mechanism we have found in 2-D study is highly dependent on the 2-D simplification itself. To verify whether the separation region can still be created and maintained by CFJ on rudder suction surface, a brief 3-D study is conducted and shown as follows.

6 Control Surface Optimal CFJ Location Study

Flowfields and performances of Baseline, Rudder-CFJ and Rudder-Stabilizer-CFJ with rudder deflection angle δ=30° are compared. The streamlines around baseline are shown in Fig. 17(a). It can be clearly seen that, the flow around the suction surface of rudder is severely separated, especially near root. Fig. 17(b)-(d) shows the Mach contour around rudder root, half height ("midspan") and tip region.

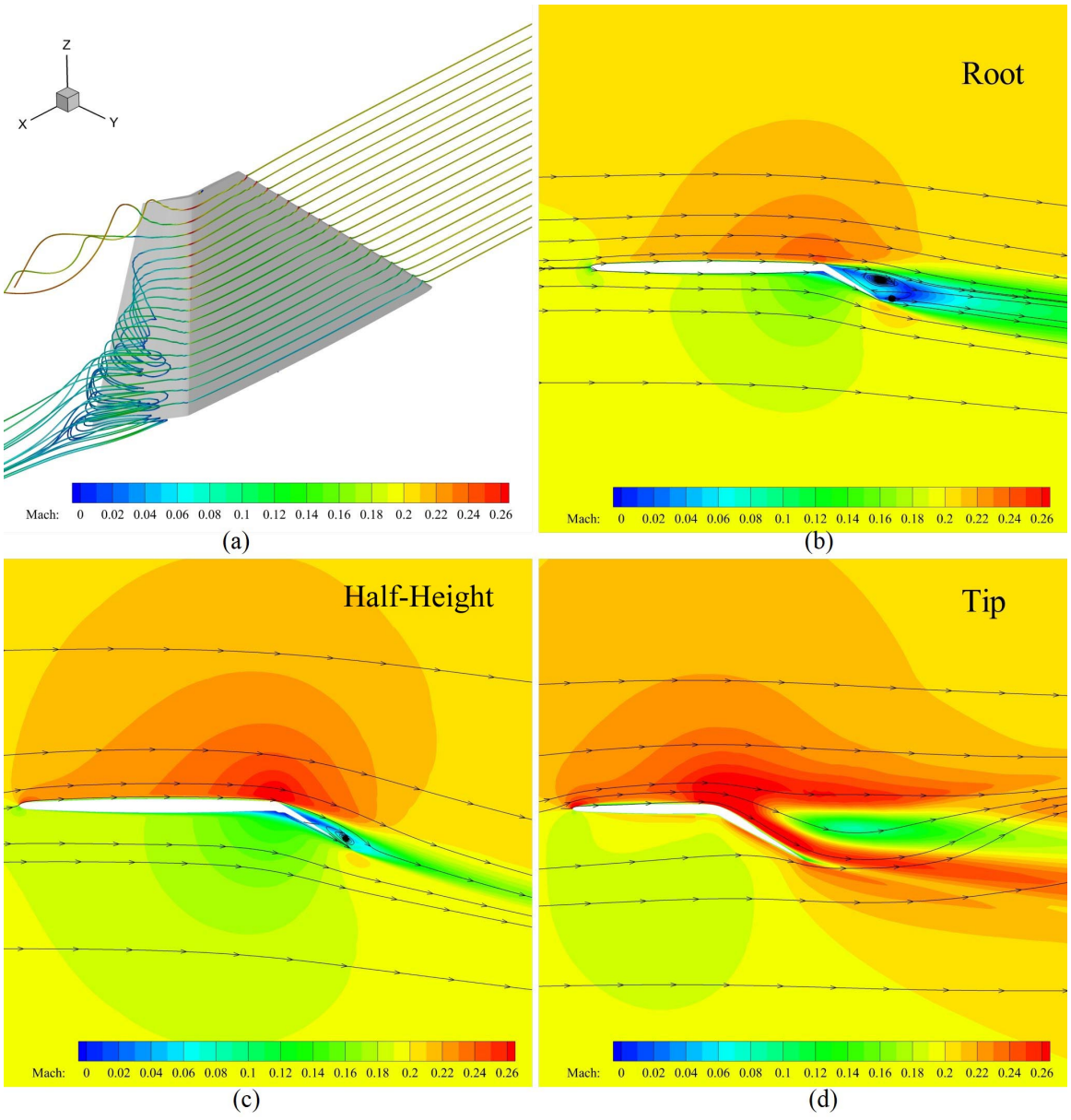

Figure 17: The streamline around baseline(a) and Mach number contours at root(b), half height(50%H)(c) and tip(d) at Mach number of 0.2.

Initial 2-D study suggests that the combination of Rudder-CFJ and Stabilizer-CFJ has the best performance while a "Stabilizer-CFJ" model cannot effectively remove the separation around rudder. However, when 3-D effect is taken into consideration, situations have become different. The streamlines around the first CFJ vertical tail,

Rudder-CFJ, are shown in Fig. 18(a). It can be seen that, with $C_\mu = 0.08$, the separation around rudder is completely wiped out, and unlike 2-D results, there is no extra separation observed near LE. Fig. 17(b)-(d) shows that, with a CFJ on rudder suction surface, the separation no longer exists near not only half height region, but also root. The streamlines around the second CFJ vertical tail model, Rudder-Stabilizer-CFJ, are shown in Fig. 20(a). The CFJ C_μ is still 0.08 in total but uniformly allocated to two CFJ sets mounted on stabilizer and rudder. It can be noticed that, different from what 2-D results indicate, the jet flow in the downstream suction surface region of stabilizer introduced some vortices near the root, which impairs the lift enhancement effect.

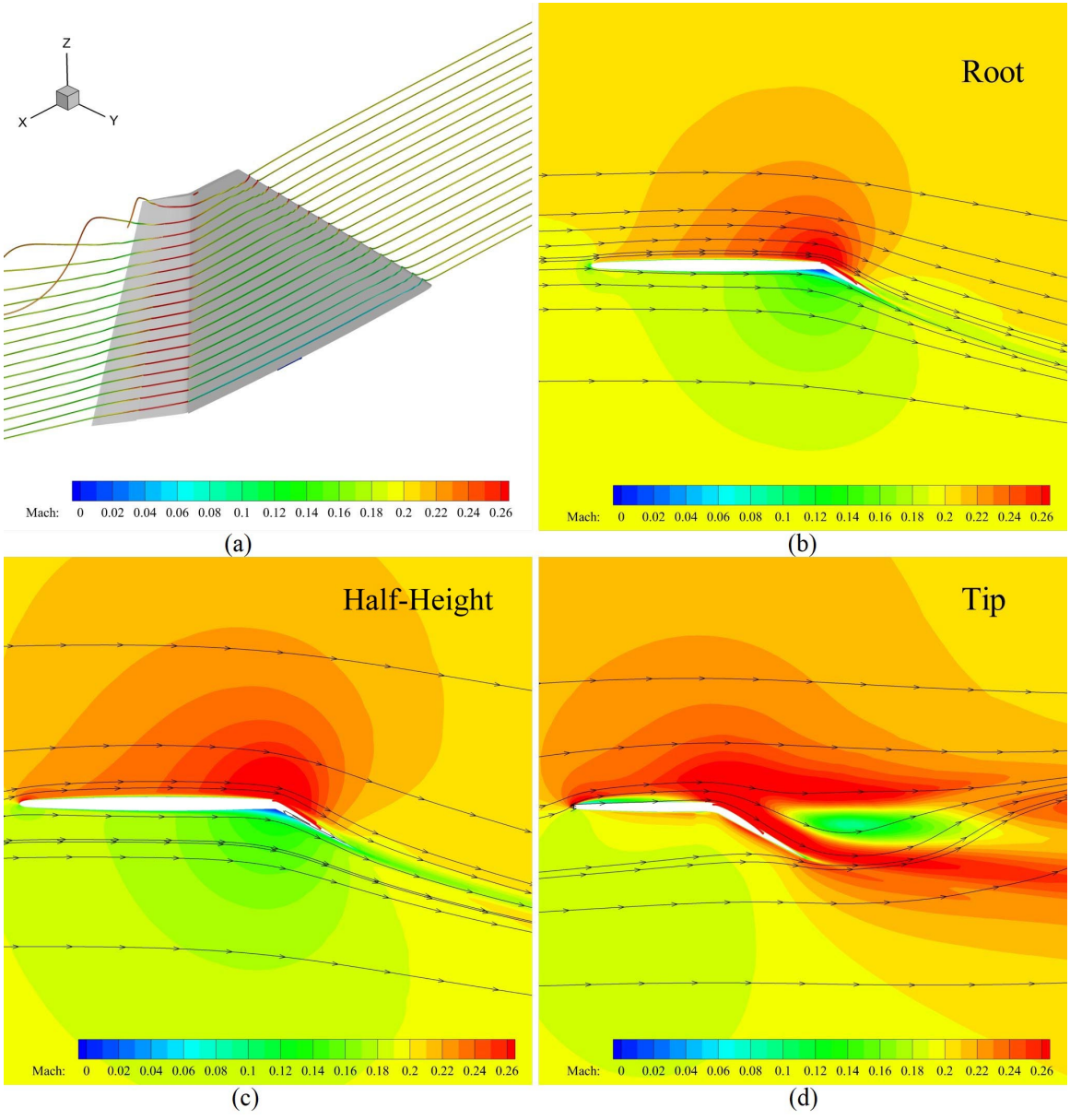

Figure 18: The streamline around Rudder-CFJ(a) and Mach number contours at root(b), half height(c) and tip(d) at Mach number of 0.2, $C_\mu = 0.08$.

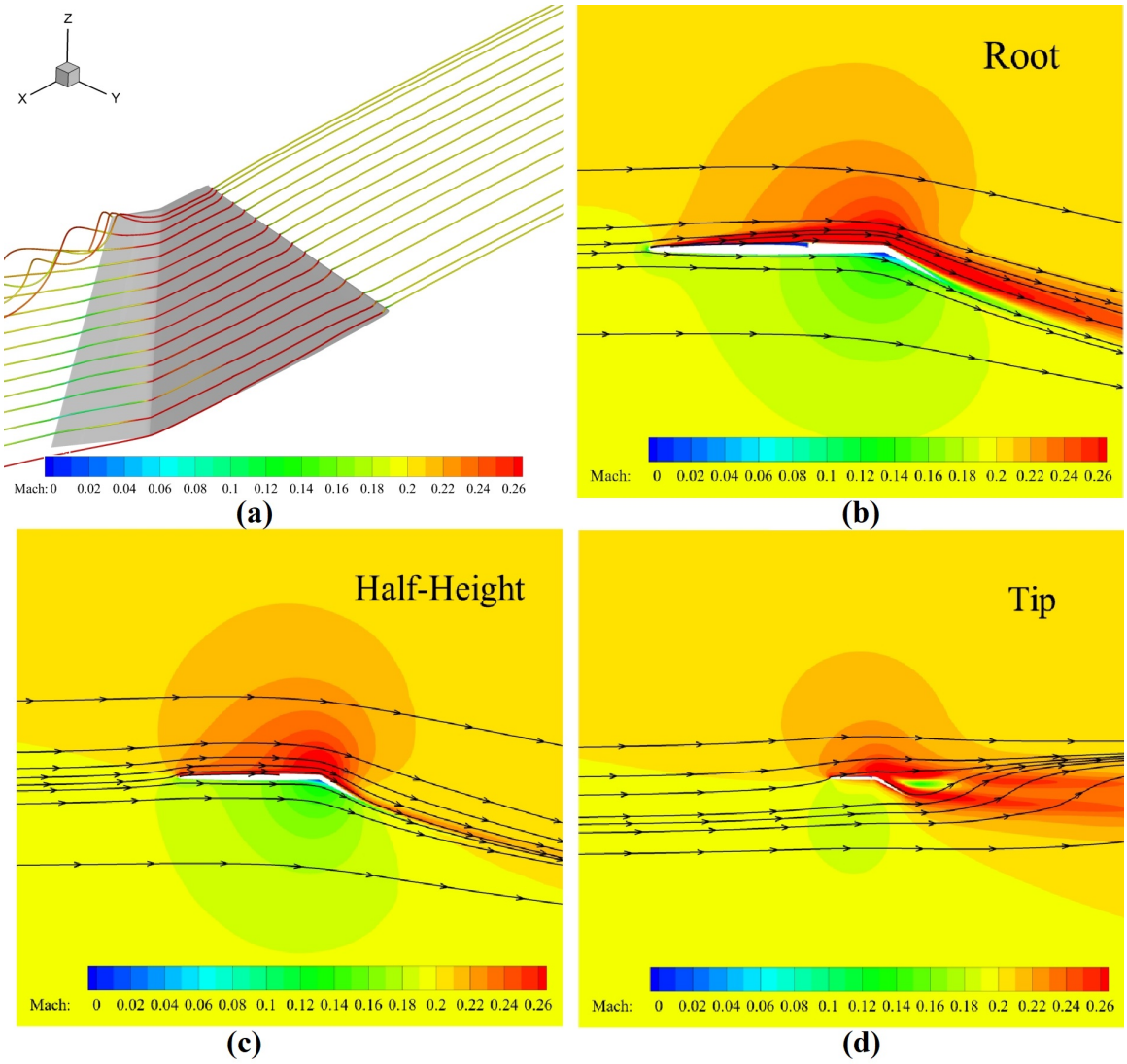

Figure 19: The streamline around Rudder-CFJ(a) and Mach number contours at root(b), half height(c) and tip(d) at Mach number of 0.2, $C_\mu = 0.08$.

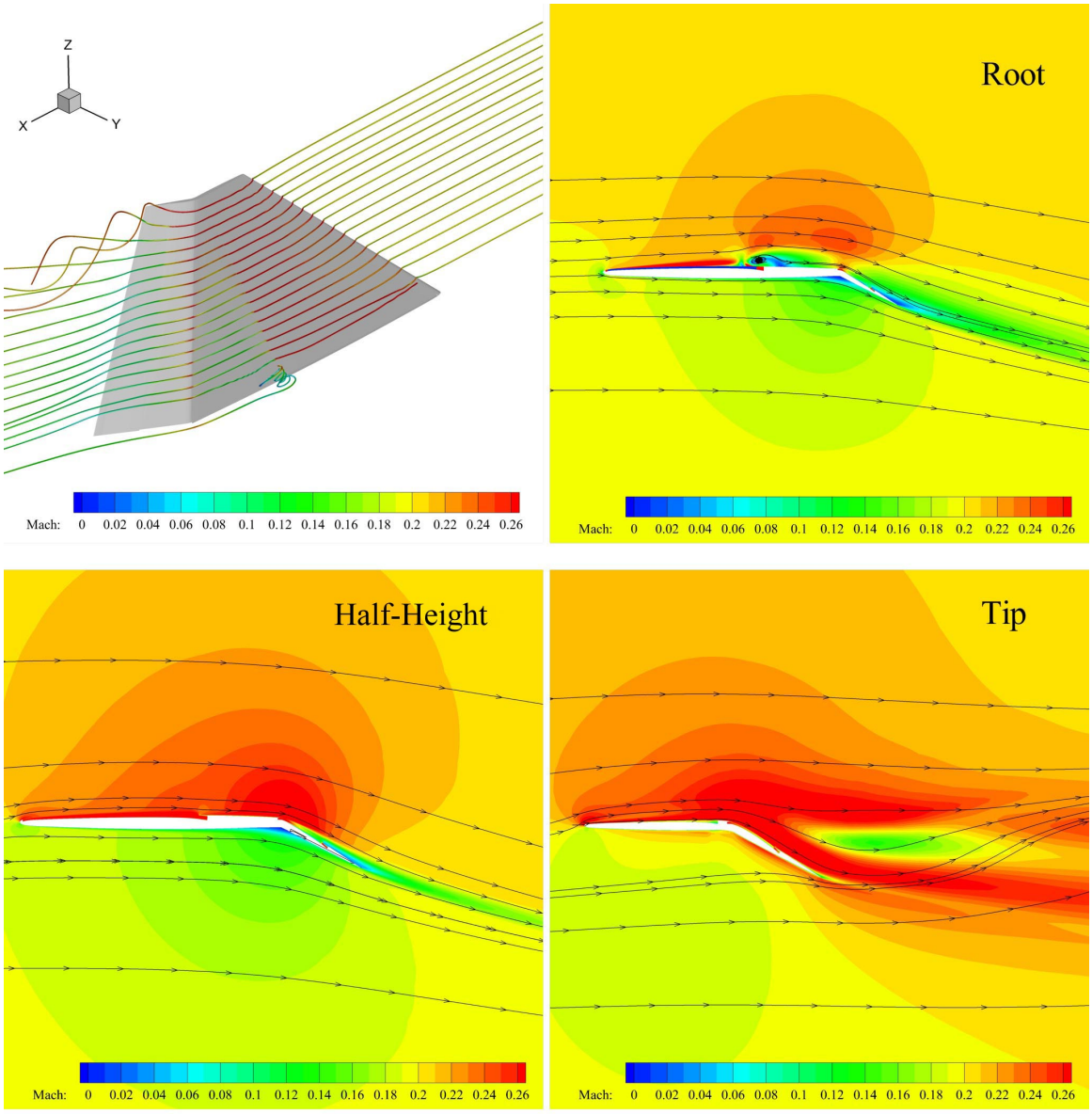

Figure 20: The streamline around Rudder-Stabilizer-CFJ(a) and Mach number contours at root(b), half height(c) and tip(d) at Mach number of 0.2, $C_\mu = 0.08$.

Comparison of isentropical Mach number at three spanwise locations between Baseline, Rudder-CFJ and Rudder-Stabilizer-CFJ models are shown in Fig. 21 below. It can be seen that, most of the pressure difference (which leads to lift increment) comes from the suction surface of rudder in a range from root to half height; the separation region near LE of stabilizer in 2-D Rudder-CFJ case no longer exists.

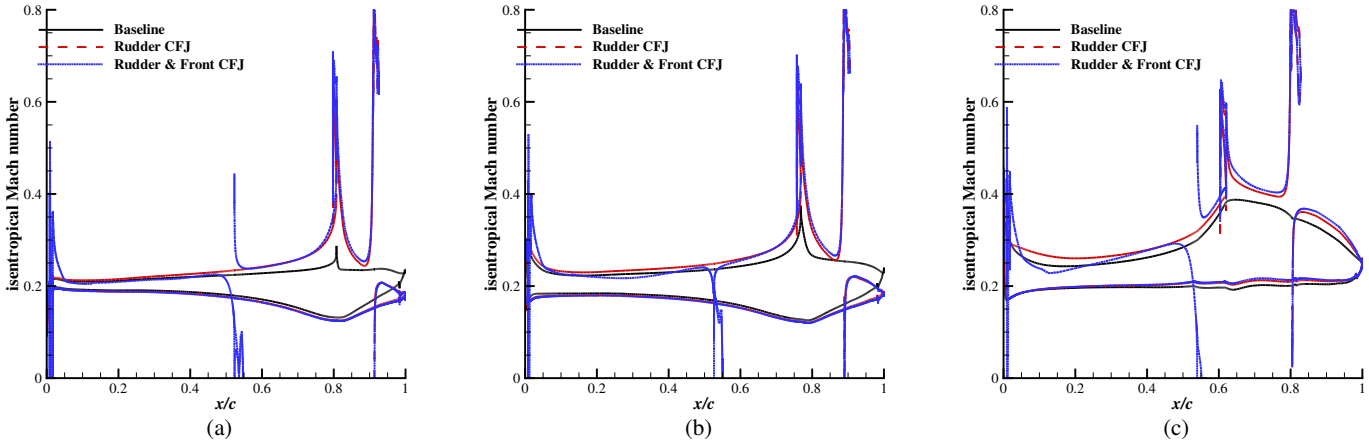

Figure 21: Comparison of isentropical Mach number distribution between root(a), half height(b) and tip(c) of baseline, Rudder-CFJ and Rudder-Stabilizer-CFJ, M=0.2, Flap deflection angle δ=30°, CFJ C_μ=0.08.

The performances of three configurations are listed in Table. 3. The result shows that, when the rudder is deflected for 30°, at a C_μ of 0.08, Rudder-CFJ can increase C_L by 30.95% at around 10% cost of corrected L/D ratio, while the combined Rudder-Stabilizer-CFJ can increase C_L by 24.9% at around twice as that cost. Since it's not typical for rudder to deflect constantly with a sideslip angle β of 0° during cruise flight, the reduce of $C_L/C_{D,c}$ is considered less crucial.

Table 3: Comparison of C_L, $C_L/C_{D,c}$ and other performances, β=0°, δ=30°, CFJ C_μ=0.08.

Type	C_L	ΔC_L	C_D	C_M	P_c	C_L/C_D	$C_L/C_{D,c}$	$\Delta C_L/C_{D,c}$
Baseline	0.685	-	0.121	0.131	0	5.661	5.661	-
Rudder-Stabilizer-CFJ	0.811	18.4%	0.127	-0.115	0.110	6.386	3.422	-39.6%
Rudder-Stabilizer-CFJ-2	0.808	18.0%	0.157	-0.246	0.075	5.147	3.483	-38.5%
Rudder-CFJ	0.906	32.3%	0.146	0.192	0.026	6.206	5.267	-7.0%
Stabilizer-CFJ	0.939	37.1%	0.136	-0.113	0.121	6.904	3.654	-35.5%

7 Conclusions

The effects using Co-Flow Jet (CFJ) active flow control method for 2-D and 3-D supersonic control surfaces with plain flaps are investigated. The 2-D and initial 3-D numerical studies indicate that, the CFJ equipped control surfaces can dramatically increase the lift coefficient and aerodynamic efficiency simultaneously compared with the original control surface with the same size of flap and deflection angle. However, due to the nature of low maximum thickness of airfoil and highly-swept planform, the 3-D effect is much stronger than the similar applications of wings with normal thickness.

In the 2-D simulation, at jet momentum coefficient of 0.08, the maximum lift coefficient is increased by 54.6% at side slip angle of 0°; when the jet momentum coefficient is increased to 0.16, the maximum lift coefficient increment is 76.5% compared with baseline. The 2-D CFJ airfoils show impressive efficiency at negative side slip angle conditions, where the maximum C_L increment compared with baseline is 157.4% at side slip angle of -7° with

C_μ of 0.08. In the 2-D simulations, the Rudder-CFJ airfoil has extra lift enhancing effect, which is achieved by forming a stable separation region near the leading edge of the stabilizer, which increases the pressure difference over there. However, this lift enhancing mechanism no longer exists when it comes to the 3-D situation. The maximum lift coefficient increment with C_μ=0.08 in 3-D simulation is 37.1%, while the smallest loss of corrected aerodynamic efficiency achieved is 7.0% with a gain of maximum lift increment of 32.3%. Similar as the results on conventional airfoils, supersonic aircraft vertical tails equipped with CFJ show impressive potential to improve the control authority at low speed.

8 Acknowledgment

The simulations are conducted on Pegasus super-computing system at the Center for Computational Sciences (CCS) at the University of Miami.

References

[1] B. L. Storms and C. S. Jang, "Lift enhancement of an airfoil using a gurney flap and vortex generators," *Journal of Aircraft*, vol. 31, no. 3, pp. 542–547, 1994.

[2] L. Pack, N. Schaeffler, C. Yao, and A. Seifert, "Active control of flow separation from the slat shoulder of a supercritical airfoil," in *1st Flow Control Conference*, p. 3156, 2002.

[3] S. Anders, W. Sellers III, and A. Washburn, "Active flow control activities at nasa langley," in *2nd AIAA Flow Control Conference*, p. 2623, 2004.

[4] G.-C. Zha, B. F. Carroll, C. D. Paxton, C. A. Conley, and A. Wells, "High-performance airfoil using coflow jet flow control," *AIAA journal*, vol. 45, no. 8, pp. 2087–2090, 2007.

[5] V. Kibens and W. W. Bower, "An Overview of Active Flow Control Applications at The Boeing Company." AIAA 2004-2624, June 2004.

[6] O. Kandil, E. Gercek, X. Zheng, and X. Luo, "Development of computational sensing and active flow control of airfoils during dynamic stall," in *42nd AIAA Aerospace Sciences Meeting and Exhibit*, p. 43, 2004.

[7] A. Lefebvre, B. Dano, W. Bartow, M. Difronzo, and G. Zha, "Performance and energy expenditure of coflow jet airfoil with variation of mach number," *Journal of Aircraft*, vol. 53, no. 6, pp. 1757–1767, 2016.

[8] T. Van Buren and M. Amitay, "Comparison between finite-span steady and synthetic jets issued into a quiescent fluid," *Experimental Thermal and Fluid Science*, vol. 75, pp. 16–24, 2016.

[9] N. W. Rathay, M. J. Boucher, M. Amitay, and E. Whalen, "Performance enhancement of a vertical tail using synthetic jet actuators," *AIAA journal*, vol. 52, no. 4, pp. 810–820, 2014.

[10] J. C. Lin, M. Y. Andino, M. G. Alexander, E. A. Whalen, M. A. Spoor, J. T. Tran, and I. J. Wygnanski, "An overview of active flow control enhanced vertical tail technology development," in *54th AIAA aerospace sciences meeting*, p. 0056, 2016.

[11] M. Y. Andino, J. C. Lin, A. E. Washburn, E. A. Whalen, E. C. Graff, and I. J. Wygnanski, "Flow separation control on a full-scale vertical tail model using sweeping jet actuators," in *53rd AIAA aerospace sciences meeting*, p. 0785, 2015.

[12] G.-C. Zha and D. C. Paxton, "A Novel Flow Control Method for Airfoil Performance Enhancement Using Co-Flow Jet." *Applications of Circulation Control Technologies*, Chapter 10, p. 293-314, Vol. 214, Progress in Astronautics and Aeronautics, AIAA Book Series, Editors: Joslin, R. D. and Jones, G.S., 2006.

[13] G.-C. Zha, W. Gao, and C. Paxton, "Jet Effects on Co-Flow Jet Airfoil Performance," *AIAA Journal, No. 6,*, vol. 45, pp. 1222–1231, 2007.

[14] G.-C. Zha, C. Paxton, A. Conley, A. Wells, and B. Carroll, "Effect of Injection Slot Size on High Performance Co-Flow Jet Airfoil," *AIAA Journal of Aircraft*, vol. 43, 2006.

[15] G.-C. Zha, B. Carroll, C. Paxton, A. Conley, and A. Wells, "High Performance Airfoil with Co-Flow Jet Flow Control," *AIAA Journal*, vol. 45, 2007.

[16] Wang, B.-Y. and Haddoukessouni, B. and Levy, J. and Zha, G.-C., "Numerical Investigations of Injection Slot Size Effect on the Performance of Co-Flow Jet Airfoil," *Journal of Aircraft*, vol. Vol. 45, No. 6,, pp. pp.2084–2091, 2008.

[17] B. P. E. Dano, D. Kirk, and G.-C. Zha, "Experimental Investigation of Jet Mixing Mechanism of Co- Flow Jet Airfoil." AIAA-2010-4421, 5th AIAA Flow Control Conference, Chicago, IL, 28 Jun - 1 Jul 2010.

[18] B. P. E. Dano, G.-C. Zha, and M. Castillo, "Experimental Study of Co-Flow Jet Airfoil Performance Enhancement Using Micro Discreet Jets." AIAA Paper 2011-0941, 49th AIAA Aerospace Sciences Meeting, Orlando, FL, 4-7 January 2011.

[19] A. Lefebvre, G-C. Zha, "Numerical Simulation of Pitching Airfoil Performance Enhancement Using Co-Flow Jet Flow Control," *AIAA paper 2013-2517*, June 2013.

[20] A. Lefebvre, G-C. Zha, "Cow-Flow Jet Airfoil Trade Study Part I : Energy Consumption and Aerodynamic Performance," *32nd AIAA Applied Aerodynamics Conference, AIAA AVIATION Forum, AIAA 2014-2682*, June 2014.

[21] A. Lefebvre, G-C. Zha, "Cow-Flow Jet Airfoil Trade Study Part II : Moment and Drag," *32nd AIAA Applied Aerodynamics Conference, AIAA AVIATION Forum, AIAA 2014-2683*, June 2014.

[22] Lefebvre, A. and Zha, G.-C., "Trade Study of 3D Co-Flow Jet Wing for Cruise Performance." AIAA Paper 2016-0570, AIAA SCITECH2016, AIAA Aerospace Science Meeting, San Diego, CA, 4-8 January 2016.

[23] J. Zhang, K. Xu, Y. Yang, Y. Ren, P. Patel, and G. Zha, "Aircraft control surfaces using co-flow jet active flow control airfoil," in *2018 applied aerodynamics conference*, p. 3067, 2018.

[24] K. Xu, J. Zhang, and G. Zha, "Drag minimization of co-flow jet control surfaces at cruise conditions," in *AIAA Scitech 2019 Forum*, p. 1848, 2019.

[25] K. Xu and G. Zha, "3d aircraft control surface enabled by co-flow jet flap," in *AIAA AVIATION 2022 Forum*, p. 3889, 2022.

[26] D. Mavris and M. Kirby, "Takeoff / landing assessment of an hsct with pneumatic lift augmentation," in *37th Aerospace Sciences Meeting and Exhibit*, p. 534, 1998.

[27] R. L. L. Englar, "Circulation control for high lift and drag generation on stol aircraft," *Journal of Aircraft*, vol. 12, no. 5, pp. 457–463, 1975.

[28] Z. Lei and G. Zha, "Lift enhancement for highly swept 3d delta wing at low speed using coflow jet flow control," in *AIAA AVIATION 2021 FORUM*, p. 2559, 2021.

[29] Z. Lei and G. Zha, "Lift enhancement of supersonic thin airfoil at low speed by co-flow jet active flow control," in *AIAA AVIATION 2021 FORUM*, p. 2591, 2021.

[30] Z. Lei and G. Zha, "Numerical investigation of low speed performance of a curved co-flow jet supersonic airfoil," in *AIAA SCITECH 2023 Forum*, p. 0243, 2023.

[31] A. Lefebvre and G-C. Zha, "Conceptual Design of an Electric Airplane Utilizing Co-Flow Jet Flow Control," *AIAA Paper 2015-0772, 53rd AIAA Aerospace Sciences Meeting*, Jan 2015.

[32] Yang, Yunchao and Zha, Gecheng, "Super-Lift Coefficient of Active Flow Control Airfoil: What is the Limit?," *AIAA Paper 2017-1693, AIAA SCITECH2017, 55th AIAA Aerospace Science Meeting, Grapevine, Texas*, p. 1693, 9-13 January 2017.

[33] Z. Liu and G. Zha, "Transonic airfoil performance enhancement using co-flow jet active flow control," in *8th AIAA Flow Control Conference*, p. 3472, 2016.

[34] Z. Lei and G. Zha, "Axis-symmetric mixed-compression supersonic inlet bleed via a zero-net-mass-flux co-flow jet flow control," in *AIAA SCITECH 2022 Forum*, p. 2234, 2022.

[35] Zha, G.C., Shen, Y.Q. and Wang, B.Y., "An improved low diffusion E-CUSP upwind scheme ," *Journal of Computer and Fluids*, vol. 48, pp. 214–220, Sep. 2011.

[36] G.-C. Zha and E. Bilgen, "Numerical Study of Three-Dimensional Transonic Flows Using Unfactored Upwind-Relaxation Sweeping Algorithm," *Journal of Computational Physics*, vol. 125, pp. 425–433, 1996.

[37] B. Corp., "Technical specs manual of concorde," 1968.

[38] Y.-Q. Shen, G.-C. Zha, and B.-Y. Wang, "Improvement of Stability and Accuracy of Implicit WENO Scheme ," *AIAA Journal*, vol. 47, pp. 331–344, 2009.

[39] Z. Lei and G. Zha, "Numerical study of co-flow-jet distribution along the span of finite wing," in *AIAA SCITECH 2023 Forum*, p. 2609, 2023.

[40] K. Xu and G. Zha, "High control authority 3d aircraft control surfaces using co-flow jet," in *AIAA aviation 2019 forum*, p. 3168, 2019.